Equilibrium drop surface profiles in electric fields

2007 J. Phys.: Condens. Matter 19 375112

(http://iopscience.iop.org/0953-8984/19/37/375112)

IOP PUBLISHING JOURNAL OF PHYSICS: CONDENSED MATTER

J. Phys.: Condens. Matter **19** (2007) 375112 (20pp) doi:10.1088/0953-8984/19/37/375112

Equilibrium drop surface profiles in electric fields

F Mugele[1] **and J Buehrle**[2]

[1] Physics of Complex Fluids, Faculty of Science and Technology, Institute of Mechanics Process and Control Twente (Impact), University of Twente, PO Box 217, 7500 AE Enschede, The Netherlands
[2] Fachbereich Physik, Philipps-Universität Marburg, Renthof 5, D-35032 Marburg, Germany

Received 19 January 2007
Published 13 August 2007
Online at stacks.iop.org/JPhysCM/19/375112

Abstract

Electrowetting is becoming a more and more frequently used tool to manipulate liquids in various microfluidic applications. On the scale of the entire drop, the effect of electrowetting is to reduce the apparent contact angle of partially wetting conductive liquids upon application of an external voltage. Microscopically, however, strong electric fields in the vicinity of the three phase contact line give rise to local deformations of the drop surface. We determined the equilibrium surface profile using a combined numerical, analytical, and experimental approach. We find that the *local* contact angle in electrowetting is equal to Young's angle independent of the applied voltage. Only on the scale of the thickness of the insulator and beyond does the surface slope assume a value consistent with the voltage-dependent apparent contact angle. This behaviour is verified experimentally by determining equilibrium surface profiles for insulators of various thicknesses between 10 and 250 μm. Numerically and analytically, we find that the local surface curvature diverges algebraically upon approaching the contact line with an exponent $-1 < \mu < 0$. We discuss the relevance of the local surface properties for dynamic aspects of the contact line motion.

(Some figures in this article are in colour only in the electronic version)

1. Introduction

Electric fields are widely used as a tool to manipulate liquids on small scales, in particular for controlling the shape, the motion, and the generation of small drops of conductive liquids [1–5]. The electric fields give rise to free and/or polarization charges at drop surfaces and thereby to mechanical forces acting on the liquid surface [6]. For sessile drops, the presence of charges and electric fields also affects the wetting properties [7–10]. The most prominent effect in this context is the electrowetting effect [4, 11, 12], which amounts to the fact that the apparent contact angle of sessile drops on partially wetting substrates can be reduced by applying an external voltage. Electrowetting has been used successfully for both fundamental

experiments in wetting science [13–16] and a variety of technological applications including liquid lenses [17–19], displays [20], and labs-on-a-chip [21, 22]. Electrowetting makes use of dc and/or low ac frequency voltages, such that electric fields are completely screened from the interior of the liquid. At higher frequencies (typically above several tens or hundreds of kilohertz), electric fields penetrate the liquid and the character of the forces becomes dielectrophoretic (see [23–25] and references therein).

Since electrowetting consists primarily of a reduction of the contact angle, there has been a tradition of explaining electrowetting in terms of a variation of interfacial energies, namely a reduction of the solid–liquid interfacial energy with increasing voltage [26]. This view dates back to early work on electrowetting, in which the wetting properties of electrolytes in direct contact with metals were investigated. Others argued that electrowetting, and in particular the now typical electrowetting-on-dielectric configuration in which an insulating layer separates the electrolyte from the electrode, should be viewed as a purely electromechanical effect [9, 27–30]. In particular, Jones [27, 29] introduced the method of calculating the Maxwell stress tensor in order to derive the electromotive forces acting in electrowetting. The former view seems to suggest that electrowetting affects primarily the force balance at the contact line, whereas the latter view stresses the pressure balance at the drop surface. Although both models predict the same variation of the contact angle and the same electromotive forces, there has been some uneasiness as to how electrowetting should be interpreted.

In two recent theoretical and numerical studies [9, 30], we demonstrated that the electromechanical approach is the fundamentally correct one. From these studies, it also becomes clear that the two views of electrowetting mentioned above are in fact consistent with each other. On small scales (i.e. scale of the order of the thickness of the insulating layer) the pressure exerted by the electric fields on the drop surface determines the local equilibrium shape. If the drop shape is only considered on a larger scale, however, it is indeed appropriate to interpret electrowetting as an effect that *effectively* reduces the solid–liquid interfacial tension (and thereby the apparent contact angle). The purpose of the present communication is (i) to provide an extended account of our earlier numerical work on equilibrium surface profiles [9] and (ii) to present experimental results testing the theoretical models. The most pertinent predictions of our theory are that (i) the local contact angle is equal to Young's angle independent of the applied voltage and that (ii) the curvature of the drop surface should diverge close to the contact line. Both aspects are confirmed by the experiments.

The paper will begin with a brief review of the basic theoretical background. After that we will discuss first our numerical results, followed by the experiments. The communication will conclude with a discussion and some remarks about open problems in the field.

2. Physical background

A detailed overview over the theoretical background of electrowetting was given in [4]. In this section, we provide a brief overview to clarify the basic physical concepts and notations that will be needed in the following. Figure 1 shows the generic geometry of an electrowetting set-up. A drop (radius R) of a partially wetting conductive liquid sits on a flat electrode, which is covered by a thin insulating layer (thickness d). The liquid is typically an aqueous salt solution. Materials are chosen such that the contact angle (Young's angle) in the absence of electric fields is rather large, $\theta_Y > 90°$ (dashed surface profile). As a voltage is applied between the liquid and the electrode the apparent contact angle decreases following the electrowetting equation

$$\cos\theta = \frac{\sigma_{sv} - \sigma_{sl}}{\sigma_{lv}} + \frac{cU^2}{2\sigma_{lv}} = \cos\theta_Y + \eta. \tag{1}$$

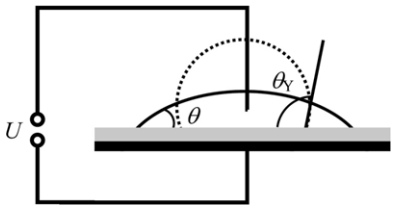

Figure 1. Schematic electrowetting set-up. The counter-electrode is shown in black at the bottom. Grey: insulating layer. Dashed line: drop profile at zero voltage. Solid line: drop profile at finite voltage.

Here, $c = \varepsilon_0\varepsilon_d/d$ is capacitance per unit area and η is the dimensionless electrowetting number. σ_{sl} and σ_{sv} are the interfacial tensions between the solid substrate and the drop phase (sl) and the ambient medium (sv), respectively. If we assume that the drop phase is perfectly conductive and the ambient medium as well as the insulating layer are perfect dielectrics, this equation can be derived either by minimizing simultaneously the surface energies and the electrostatic energy, or by balancing the net forces acting on the contact line, as described in [4]. (In the appendix we provide a quantitative derivation of the electrowetting number taking into account explicitly the distribution of ions inside the drop phase. The calculation shows that the perfect conductor assumption is usually valid.) Common to both approaches is the fact that they ignore the microscopic details of the electric field distribution close to the contact line. Vallet *et al* [31] pointed out for the first time that the electric field $\vec{E}$ in EW diverges within a region of order d around the contact line. Hence equation (1) is only valid on a scale larger than d. In typical EW applications, the drop size R is of the order of tens to hundreds of micrometres whereas d is of the order of one micrometre or less. Thus equation (1) does indeed describe the global morphology of the drop correctly.

The local morphology of the drop surface however does depend on the distribution of the electric field and of electric charges in the system. As noted above, we assume that the drop phase is perfectly conductive, i.e. the Debye screening length $\kappa_D^{-1} \approx$ O(1 nm) of the drop phase is considered to be much smaller than d. Hence, $\vec{E} = 0$ inside the drop and $(\vec{E}\cdot\vec{t})_{surf} = 0$, i.e. the electric field is oriented perpendicular to the surface ($\vec{t}$ is a local tangent vector at the drop surface). In this case the electric field gives rise to a Maxwell stress

$$\Pi_{el}(\vec{r}) = \frac{\varepsilon_0}{2}\vec{E}(\vec{r})^2 \tag{2}$$

pulling on the liquid surface along the outward normal. Beyond a certain threshold voltage, it can even lead to an instability and to the ejection of satellite droplets [31, 32]. Below the threshold voltage, the drop surface is in mechanical equilibrium if

$$\Delta P = 2\sigma_{lv}\kappa(\vec{r}) - \Pi_{el}(\vec{r}). \tag{3}$$

Here, ΔP is the pressure difference between the interior of the drop and the ambient phase and $P_L = 2\sigma_{lv}\kappa$ is the Laplace pressure, where $\kappa = (1/R_1 + 1/R_2)/2$ is the mean curvature of the liquid–vapour interface. (R_1 and R_2 are two principal radii of curvature at $\vec{r}$.)

Solving equation (3) for κ and thus for the drop shape requires the exact distribution of the electric field, which itself depends on the drop shape. Hence both the drop shape and the electric field distribution have to be calculated in a self-consistent manner. Furthermore, the equilibrium surface profile has to satisfy a Young-type force balance equation right at the contact line (i.e. at $y = 0$). Taking into account a possible contribution f_{el} due to the diverging electric fields, this equation reads

$$\sigma_{sl} + \sigma_{lv}\cos\theta = \sigma_{sv} + f_{el}. \tag{4}$$

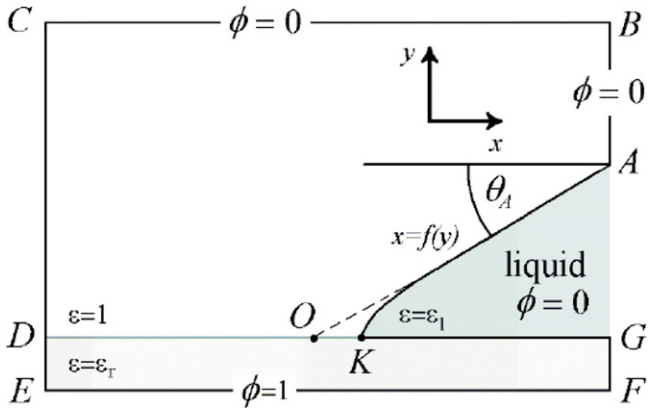

Figure 2. Geometry of the computational box and electrical boundary conditions for numerical analysis. Point A is fixed. (Not to scale. See text for details.)

Later we will show that $f_{el} = 0$ and thus $\cos\theta = \cos\theta_Y$, independent of the applied voltage.

To solve for the equilibrium drop shape, we followed a self-consistent numerical approach for arbitrary field strength. For the sake of simplicity, we restricted ourselves to two-dimensional systems, i.e. drops with $R = \infty$.

3. Numerical surface profiles

3.1. Numerical scheme

Figure 2 displays the geometry under consideration. The liquid occupies the space AKG. The point O denotes the position of the contact line at zero voltage. We consider a situation in which the liquid surface is pinned at the fixed point A on the right-hand side of the simulation box. Furthermore, we assume that the curvature is zero far away from the contact line. Upon applying a voltage, the drop surface and the contact line position K move freely, which implies a variation of the drop volume. We split the numerical task into two steps. In the first one, we determine surface profiles that satisfy the local force balance for a parameter set (θ_A; η). (Note that the profiles obtained in this first step correspond to physical systems with variable θ_Y.) In the second step, we calculate for each of these mechanically equilibrated profiles the total energy consisting of both the electrostatic energy and the surface energy. To identify the physically realized equilibrium profiles, we determine the Young angle θ_Y that minimizes the total energy for each pair (θ_A, η).

Step one consists of the iterative calculation of mechanically equilibrated surface profiles. Since d is the only length scale in the problem, all lengths will be reported in units of d. Similarly, the electrostatic potential Φ will be normalized by the applied voltage U. In these units, the Maxwell stress is given by $\Pi_{el}(\vec{r}) = \eta(\nabla\Phi)^2/\varepsilon_d$. Φ satisfies the Poisson equation

$$\nabla \cdot (\varepsilon(\vec{r})\nabla\Phi) = 0 \tag{5}$$

everywhere outside the drop. Apart from the boundary conditions specified in figure 2, we specified

$$\Phi_{CDE}(y) = \frac{1}{1+\varepsilon_d}\begin{cases} \varepsilon_d - y; & -1 \leqslant y \leqslant 0 \\ \varepsilon_d(1 - y/L_{CD}); & 0 \leqslant y \leqslant L_{CD} \end{cases} \tag{6}$$

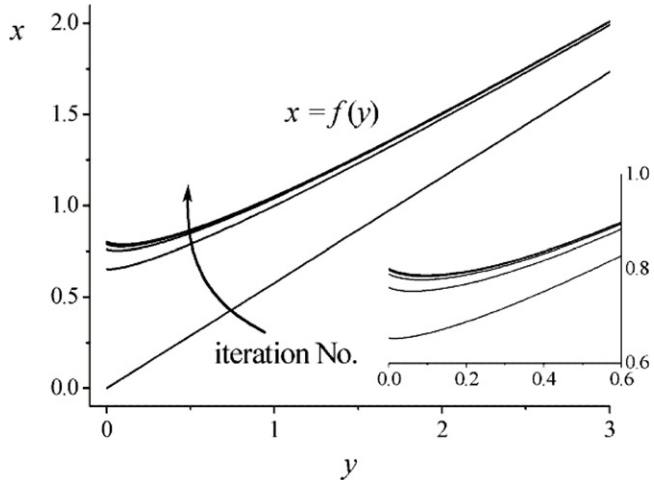

Figure 3. Convergence of drop profiles during the first ten iterations (parameters: $\eta = 1$; $\varepsilon_d = 1$; $\theta_A = 60°$). Inset: zoomed view close to point K.

along CDE (with L being the distance CD) and a Neumann condition along AGF. The size of the numerical box was chosen to be BC = CD = 80 and AG = 40 for most calculations. A larger box size was used for the lowest values of θ_A. Several test calculations were performed to verify that the results were independent of the box size.

If we represent the liquid surface as a function $x = f(y)$, the curvature in two dimensions is given by $\kappa_{2D} = f''/(1 + f'^2)^{3/2}$, where the primes indicate a derivative w.r.t. y. With this definition the analogue of equation (3) reads

$$\sigma_{lv} \frac{f''}{(1 + f'^2)^{3/2}} = \frac{\eta}{\varepsilon_d} (\nabla \Phi)^2. \tag{7}$$

Our iterative numerical procedure consists of the following: first, we fix an asymptotic angle θ_A and choose a wedge shaped surface profile (AOG) as initial surface configuration. Second, we calculate the electric field distribution for this configuration using a finite element method, as implemented in the commercial program package Matlab. We used an adaptive grid, which gives rise to a particularly high density of grid points close to the contact line. In a typical run, we used 400 000 grid points in order to reduce the maximum deviation between the numerical data and the known analytical solution for the wedge case to less than 10^{-4}. Close to the contact line the distance between two grid points was of order 10^{-5}.

Once the electric field distribution was sufficiently converged, we integrated equation (7) starting from point A, where the Maxwell stress vanishes down to the contact line. The vertical position of point A and the fixed asymptotic angle θ_A were used as boundary conditions for the numerical integration that was performed with a Runge–Kutta routine, also as implemented in Matlab. The resulting refined surface profile was used as an input for the calculation of the electric field distribution in the next iteration. Figure 3 shows a typical iterative set of profiles. Typically, convergence was achieved in less than ten iterations. Profiles were determined for a large set (>40) of asymptotic angles θ_A ranging from 6° to 70°. (For the lowest values, the size of the numerical box was increased to 500 in order to avoid numerical artefacts.) For each asymptotic angle, the value of η was varied between 0 and 1 at a spacing of 0.2.

The surface profiles thus achieved represent mechanical equilibrium shapes for a given set of parameters ε_d, η, and θ_A. In order to establish a relation between θ_A and the Young angle θ_Y

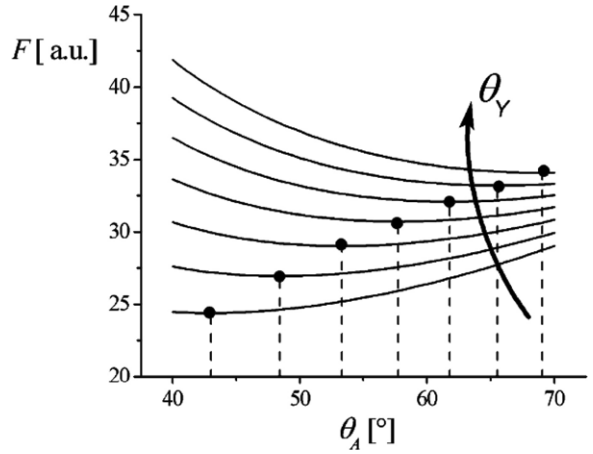

Figure 4. Free energy versus θ_A for $\theta_Y = 105, 109°, 113°, \ldots, 129°$. The minimum of each curve indicates pairs of corresponding equilibrium angles $\theta(U) - \theta_Y$.

of a given physical system, we calculated the free energy F of the system (in units of $\sigma_{lv}d^2$) consisting of both surface energies and electrostatic energy:

$$F(\varepsilon_d, \eta, \theta_A) = -L_{KG}\cos\theta_Y + \int_K^A dS - \frac{\eta}{\varepsilon_d}\int_{V_1} dV\,(\nabla\Phi)^2 - \eta\int_{V_2} dV\,(\nabla\Phi)^2. \quad (8)$$

Here, L_{KG} is the length of the solid–liquid interface. The second term represents the surface energy of the drop. This form of the free energy implies that we assume the interfacial tensions σ_i to be voltage independent. The last two terms represent the electrostatic energy inside the dielectric layer (V_1) and outside (V_2), respectively. In figure 4 we plot F as a function of θ_A for a series of values of θ_Y at a specific fixed value of η. For each value of θ_Y, F displays a minimum at a certain value of θ_A. This combination $\theta_Y - \theta_A$ corresponds to the equilibrium drop configuration for all the parameters ε_d, η, θ_A, and θ_Y.

3.2. Numerical results

We now discuss the results obtained from the procedure described above. Figure 5 shows the correlation between θ_Y and the equilibrium value of θ_A for the largest value of η ($= 1$). The solid line represents the equation $\cos\theta_A = \cos\theta_Y + \eta$. Thus we obtain as a result of our calculations that the equilibrium value of θ_A is related to the Young angle by the electrowetting equation (equation (1)). Note that this relation is fulfilled down to the lowest value of $\theta_A = 6°$ and up to a value of $\eta = 1$. In this two-dimensional system we find thus absolutely no indication of contact angle saturation.

In figure 6 we show a number of profiles for various values of η for a fixed asymptotic angle of $\theta_A = 60°$, i.e. the profiles correspond to different physical systems with variable values of θ_Y, as indicated in the figure caption. The profiles in figure 6(a) correspond to a dielectric layer with $\varepsilon_d = 1$, the ones in (b) to $\varepsilon_d = 2$. Obviously the curvature of the profiles increases upon approaching the substrate level $y = 0$, in agreement with the expectation that the electric field and thus the Maxwell stress increases upon approaching the contact line. Furthermore, the higher η, the larger the curvature of the profiles—in agreement with the expectation that higher voltages should give rise to stronger electric fields. Another practically important observation

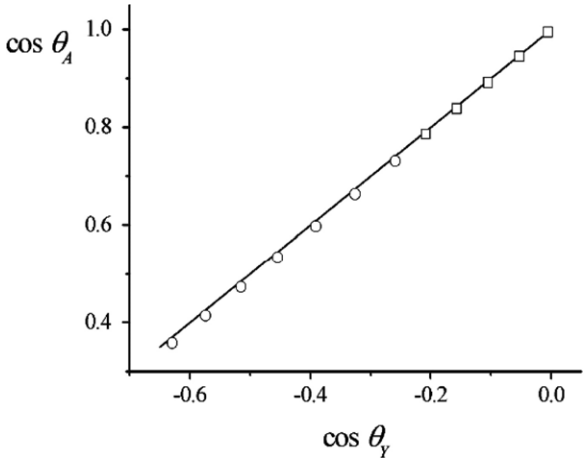

Figure 5. Pairs of equilibrium angles $\theta(U) - \theta_Y$ ($\eta = 1$). The solid line indicates the expectation based on equation (1).

is that the field-induced curvature is essentially concentrated to the region $y \leqslant 1$. Above that level, the slope of the surface is so close to its asymptotic value corresponding to θ_A that the deviation is barely noticeable—certainly from an experimental perspective. Comparing figures 6(a) and (b) it also becomes apparent that the field effect is significantly reduced for higher values of ε_d. This reduction is obviously related to the enhanced screening due to the substrate polarizability, which focuses the electric field lines close to the contact line.

To analyse the slopes of the profiles in more detail, we introduce the normalized derivative

$$\chi = \frac{f'(y) - \cot\theta_Y}{\cot\theta_A - \cot\theta_Y}, \tag{9}$$

which has the property that $\chi \to 0$ for $f' \to \cot\theta_Y$ and $\chi \to 1$ for $f' \to \cot\theta_A$. Figures 7(a) and (b) show χ corresponding to the dielectric constants of $\varepsilon_d = 1$ and 2, as in figures 6(a) and (b). Far above the substrate, the slope thus approach a value corresponding to the asymptotic angle θ_A, as expected. Close to the contact line, however, all profiles converge (within the numerically accessible range) towards a slope corresponding to θ_Y. We find thus that the local contact angle remains equal to θ_Y, independent of the applied voltage. This finding implies that the electric contribution f_{el} to the force balance at the contact line (equation (4)) vanishes.

To analyse this result further, we plot in figure 8 the square of the electric field strength, which is proportional to both the Maxwell stress and the local surface curvature. Far away from the contact line (for $y \gg 1$), there is an algebraic region with a slope -2, which corresponds simply to the result of basic electrostatics $|\vec{E}| \propto 1/y$ for a wedge with different electric potentials on the both sides. In this region the thickness of the dielectric layer is negligible. For $y \approx 1$, a cross-over takes place with a complex distance dependence. For $y \ll 1$, yet another algebraic regime is entered, however with a weaker slope. In figure 9 we display the exponent ν of this algebraic law as a function of the local contact angle α, which we have by now identified with θ_Y. The symbols are obtained by fitting to numerical pressure data, like those shown in figure 8. Clearly, the distance dependence becomes weaker with increasing contact angle.

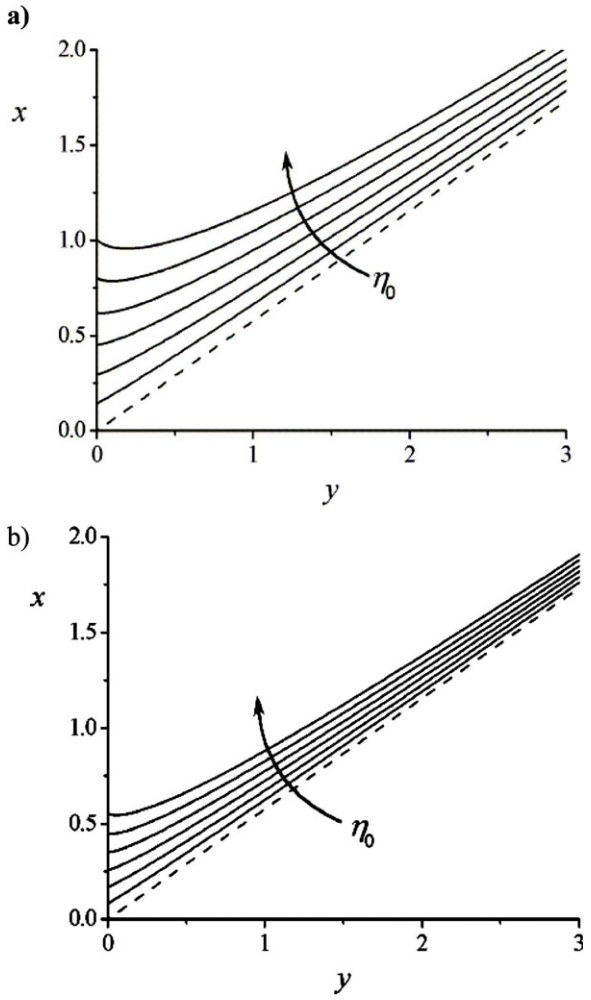

Figure 6. Equilibrium profiles for $\theta_A = 60°$ and $\eta = 0.2, 0.4, \ldots, 1$ (solid) and $\eta = 0$ (dashed). (The Young angles for the solid profiles are $\theta_Y = 72.5°$, 84.3°, 95.7°, 107.5°, and 120°, respectively.) (a) $\varepsilon_d = 1$; (b) $\varepsilon_d = 2$.

The exponent of the algebraic behaviour close to the contact line can be understood in terms of electrostatics. On such small scales, the substrate electrode is so far away that its presence can be neglected (see inset figure 9). In that case, the electrostatic potential can be written as a superposition of algebraic modes

$$\Phi = \sum_n a_n \phi_n, \tag{10}$$

with

$$\phi_n = r^{\mu_n} \begin{cases} \dfrac{\sin \mu_n(\pi - \alpha)}{\sin \mu_n \pi} \sin \mu_n \varphi; & 0 < \varphi < \pi \\ \sin \mu_n(2\pi - \alpha - \varphi); & \pi < \varphi < 2\pi - \alpha. \end{cases} \tag{11}$$

This solution fulfills the boundary conditions $\Phi = 0$ at $\varphi = 0$ and at $\varphi = 2\pi - \alpha$. The boundary condition that the normal component of the dielectric displacement has to be

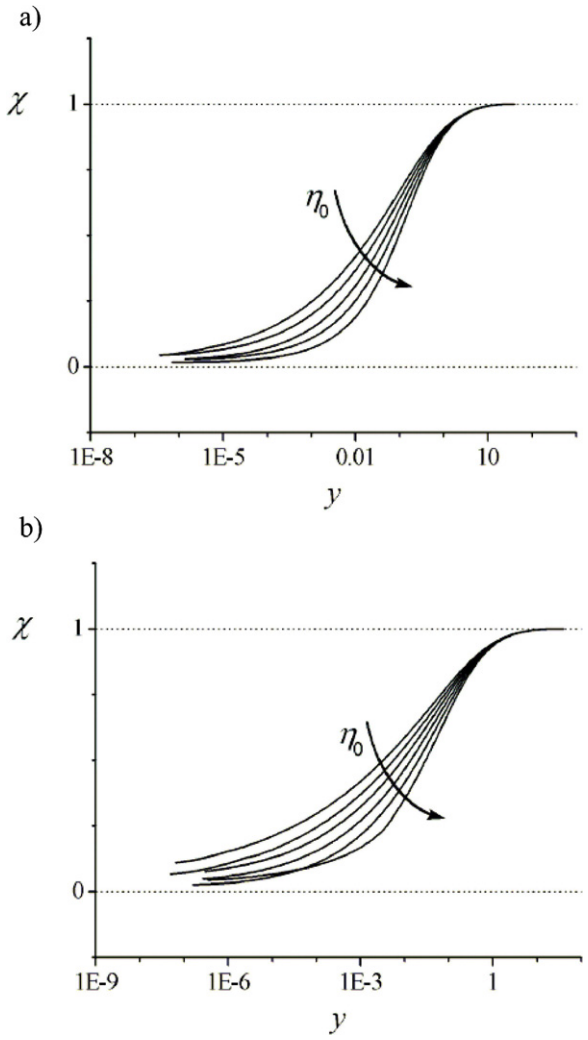

Figure 7. Normalized slopes versus height above the substrate. Same data set as figure 6.

continuous at $\varphi = \pi$ leads to the additional requirement

$$\varepsilon_v \tan \mu_n \pi + \varepsilon_d \tan \mu_n (\pi - \alpha) = 0, \tag{12}$$

where ε_v is the dielectric constant of the ambient medium, which was taken to be unity in the numerical calculations. Since $\Phi \to 0$ for $y \to 0$ the lowest mode $n = 1$ dominates for $y \ll 1$. Inserting physically reasonable values of α between zero and π into equation (12) one finds that

$$1/2 < \mu_1 < 1. \tag{13}$$

The numerical solution of equation (12) is found to confirm the numerical results presented in figure 9 (see solid lines). This result implies that the Maxwell stress $\Pi \propto (\nabla\Phi)^2$ and thus the curvature of the equilibrium surface profile also diverge algebraically with an exponent

$$-1 < \nu < 0. \tag{14}$$

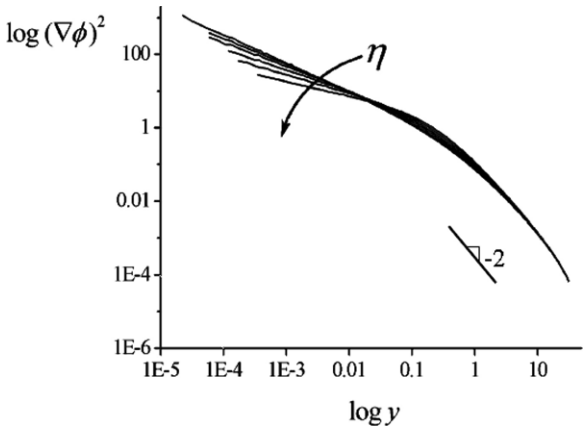

Figure 8. $(\nabla\phi)^2 \propto \Pi_{el}$ versus height. Note the cross-over between two algebraic regimes for $y \gg 1$ with an exponent -2 and for $y \ll 1$ with a θ_Y-dependent exponent (data derived from figure 6(a)).

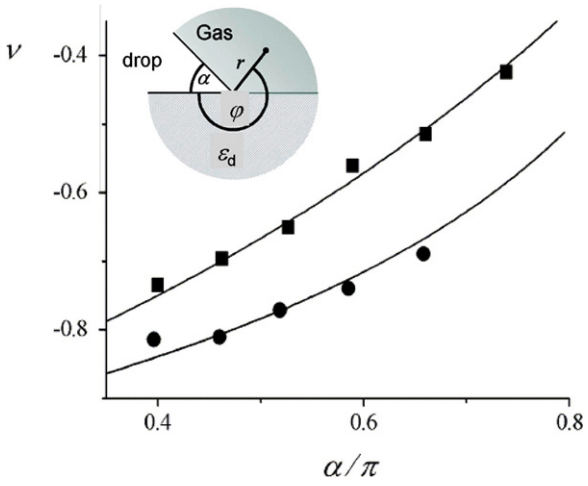

Figure 9. Algebraic exponent ν versus opening angle α $(=\theta_Y)$.

3.3. Discussion of numerical results

Using the result of equation (14), one can actually show that the electrostatic contribution f_{el} to the force on the contact line actually vanishes. To see this, we note that

$$f_{el} \propto \lim_{\delta h \to 0} \int_0^{\delta h} (\nabla \Phi)^2 \, dy \propto \lim_{\delta h \to 0} \delta h^{\nu+1} = 0. \tag{15}$$

The divergence of Π is thus so weak that the net remaining force at the contact line vanishes. Since only surface tension forces act on the contact line it is natural that the local contact angle is indeed equal to θ_Y, independent of the applied voltage.

As expected on dimensional grounds electric field-induced surface distortions are concentrated in a region of order d around the contact line. On larger scales, the apparent contact angle follows the electrowetting equation, equation (1). From a practical perspective,

figures 6–8 indicate that substantial deviations from the macroscopic behaviour can only be expected for $z \leqslant 0.1d$, in particular for larger values of ε_d.

We note here that a similar result can also be obtained in a rigorous analytical manner using conformal mapping. Unfortunately, this calculation is restricted to small voltages. The method requires the knowledge of a mapping function, which transforms the arbitrarily shaped drop surface into a simpler geometry. Our approach in [30] makes use of the well known mapping function for the undisturbed straight wedge profile in order to calculate the field distribution in the transformed coordinate system. The resulting distortion of the surface profile can then be expressed in terms of the Eulerian beta function and the hypergeometric function. In this approximation, the local contact angle is analytically found to be voltage independent, in agreement with the results described above. For $y \ll 1$, the same algebraic behaviour is found as above with identical exponents even for large values of η. This agreement seems surprising at first glance, since the approach is only valid for small η. The reason behind this agreement is, however, that the conformal mapping approach also produces wedge shaped surface profiles for $y \ll 1$ with an opening angle $\alpha = \theta_Y$. In this case, the correct algebraic exponent arises automatically—independent of the value of η. Substantial differences between the two approaches can only be expected in the transition region around $y \approx 1$.

4. Experimental surface profiles

4.1. Experimental techniques

Experiments were performed with aqueous drops immersed in a silicone oil bath (AK 5; Wacker). In order to assure perfect conductivity, salt (NaCl) was added to the water to achieve an electrical conductivity of ≈1 mS cm^{-1}. The substrates were commercial Teflon foils (Goodfellow) of variable thickness (10–250 μm) deposited on an ITO-coated glass slide. According to the specifications the dielectric constant of the Teflon films was $\varepsilon_d = 2.1$. (To assure a constant insulator thickness, a small amount of salt water was placed between the ITO glass and the Teflon film.) The contact angle (Young's angle) and the contact angle hysteresis in the absence of voltage were ≈170° and <5°, respectively. A drop size of the order of 1 mm was chosen, well below the capillary length $\kappa = (\sigma_{lv}/(g\,\Delta\rho))^{1/2}$, where g is the gravitational acceleration and $\Delta\rho = 0.2$ g cm^{-3} is the density difference between the liquid and the surrounding oil. A Pt wire with a diameter of 250 μm was immersed into the drops in order to apply a dc voltage ranging from 0 to ≈800 V. Drops were imaged from the side using a 5× microscope objective (Nikon) in combination with a zoom lens and a CCD camera.

4.2. Experimental results

Figure 10 shows a number of water drops in ambient oil for various values of the applied voltage on three different substrates with a thickness d of 10 (panels (a)–(c)), 50 ((d)–(f)), and 150 μm ((g)–(i)), respectively. Clearly, the drops are almost perfectly spherical with a Young's angle of approximately $\theta_Y = 170°$ at zero voltage. Upon increasing the voltage, the apparent contact angle decreased for all values of d. While the drop profile essentially retain their spherical cap shape all the way down to the substrate for the thinnest dielectric layers, clear deviations are seen for the thicker dielectrics at high voltage. In figure 11 we show a zoomed view of the drop profiles in the vicinity of the contact line. Panels (a)–(c) correspond to $d = 10$, 50 and 150 μm, respectively, indicated by the white bars. All pictures were taken at roughly the same value of the electrowetting number $\eta \approx 1$. These images clearly demonstrate that surface profile distortions do indeed occur on a length scale given by the thickness of the

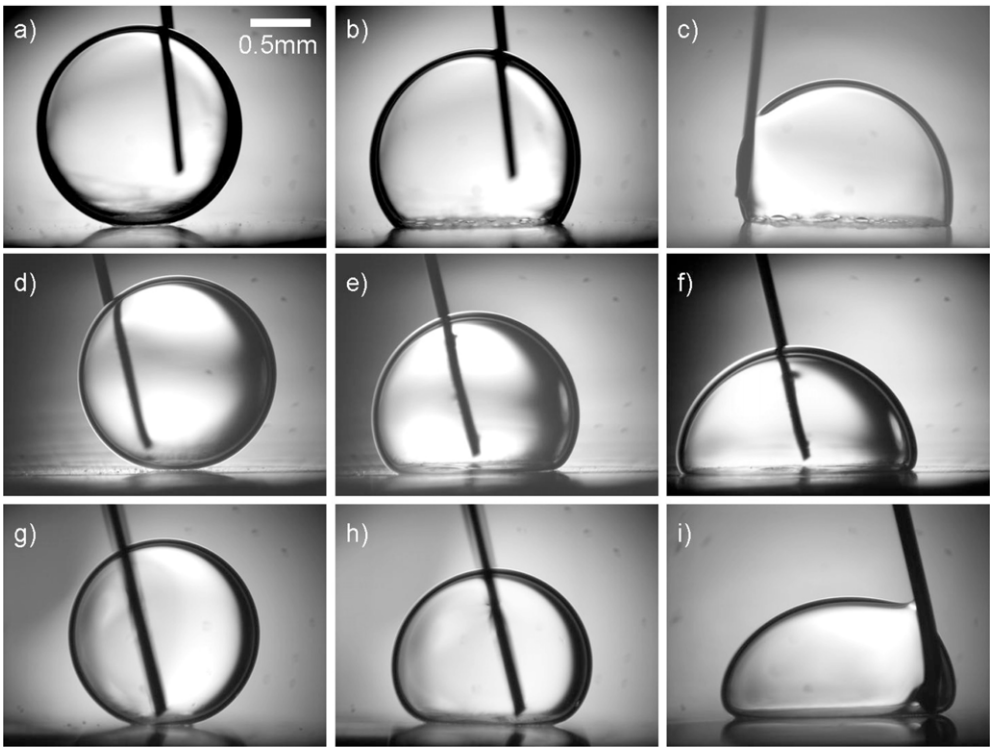

Figure 10. Video images of drops for variable voltage corresponding to $\eta \approx 0$, 0.5 and 1 (left to right) and variable substrate thickness $d = 10$, 50 and 150 μm (top to bottom).

dielectric. Panels (d)–(f) were recorded at variable $\eta = 0$, 0.5 and 1, respectively, for constant $d = 150\ \mu$m. Obviously, the local slope close to the contact line remains constant close to 170°, as indicated by the dotted white lines. Thus two main predictions of the theoretical model are confirmed directly by the experimental raw data.

To obtain a complete picture, we acquired drop profiles over a range of $0 < \eta < 1$ for all substrates and extracted the droplet contours from the images. First, we determined the apparent contact angle. To do so, we fitted circles to the surface profiles sufficiently far away from the contact line (i.e. at distances $z > d$; see figure 12). These circles were extrapolated down to the substrate to obtain the apparent contact angle. The resulting electrowetting curve is shown in figure 13. The contact angle indeed decreases in accordance with the macroscopic expectation (equation (1)); however, the obtained slopes are systematically smaller than expected (see figure caption). We attribute these deviations to an imperfect coupling between the ITO electrode and the Teflon films. Possibly ambient oil wetting the Teflon (partially) crept underneath the dielectric layer and replaced the thin salt water layer that was originally placed there to insure good electric coupling. Obviously, this would affect in particular the data for the thinnest dielectric layers. For $d = 250\ \mu$m, the drops were frequently moving laterally at high voltage such that no reliable data could be obtained for $\eta > 0.3$.

In figures 14 and 15, we show the surface profiles and the local slopes as a function of the height z above the substrate. (Note that we deliberately use a different symbol than in the two-dimensional case of the numerical simulations.) The profiles shown in figure 14 are sixth order polynomial fits to the experimental data. This fitting procedure was found to be

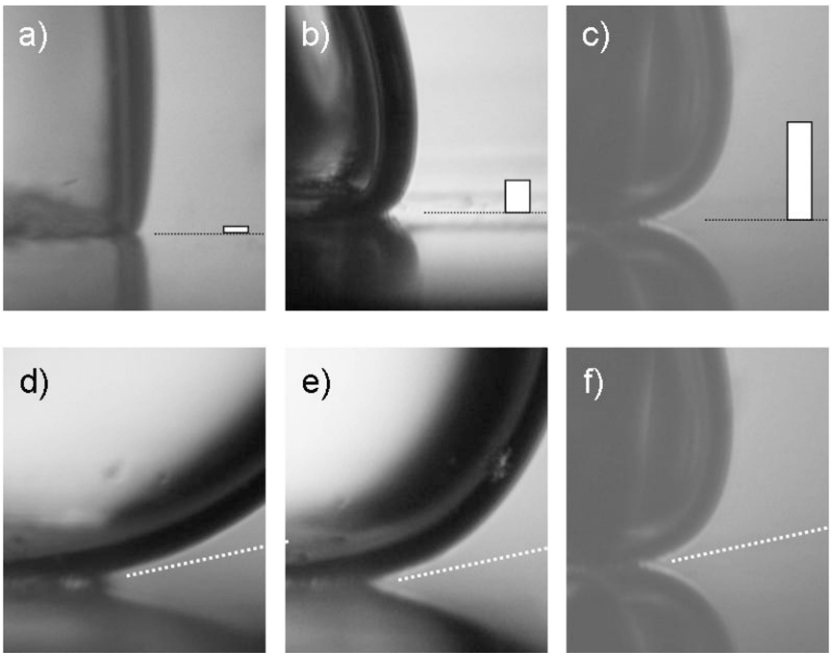

Figure 11. Close-up views of the contact line region. (a)–(c) $\eta = 1$; $d = 10$, 50 and 150 μm, as indicated by the vertical white bars. The black dotted line indicates the substrate level. (d)–(f) $d = 150$ μm; $\eta = 0$, 0.5 and 1. The white dotted lines have identical slopes.

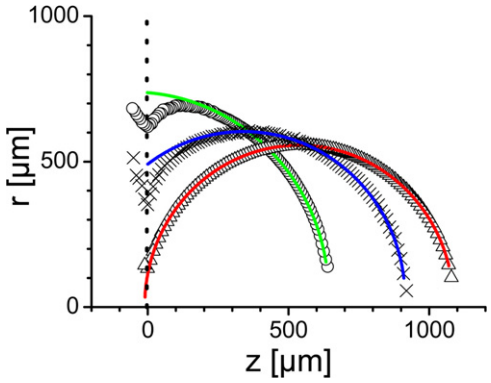

Figure 12. Drop surface profiles for $d = 150$ μm at variable voltage ($\eta = 0.06$ (triangles), 0.4 (crosses), 0.9 (circles)). Symbols indicate experimental profiles, solid lines show circles fitted to the upper part of the profiles. (For the sake of clarity only every tenth data point is shown.)

satisfactory w.r.t. both reduction of noise and simultaneously high fit quality (see panel (c)). With the polynomial fits at hand, the local surface slopes can be computed easily without excessive numerical noise as it frequently appears during numerical differentiation of discrete data. In figure 15, we plot the slope angles w.r.t. the vertical direction, such that the value at the $z = 0$ is equal to the local contact angle. The data clearly confirm the expected trend: for thin insulating layers, the slope angle close to the substrate decreases essentially along with the apparent macroscopic contact angle because our optical resolution is insufficient to resolve

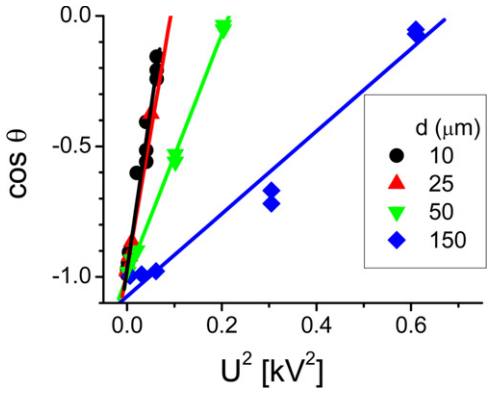

Figure 13. Electrowetting curve: cos θ versus applied voltage squared for variable nominal substrate thickness as indicated. The thickness values determined from the linear fit curves are 22, 26, 59 and 172 μm, respectively.

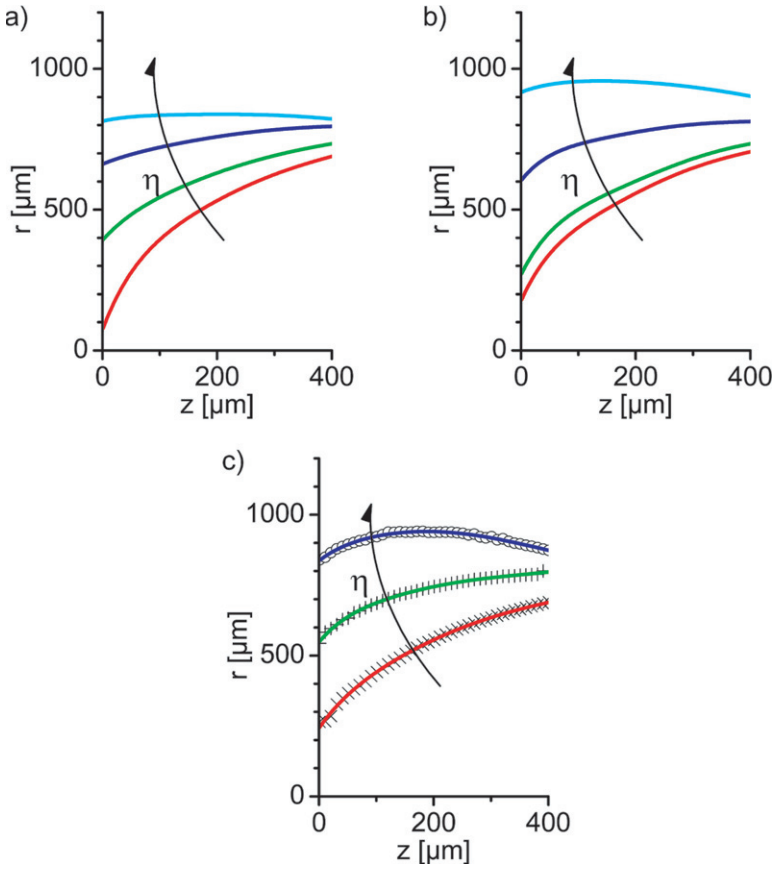

Figure 14. Surface profiles for various voltages and $d = 10$ μm (a), 50 μm (b), and 150 μm (c). Data correspond to $\eta = 0.06$, 0.3, 1.1, 1.7 (a); $\eta = 0$, 0.1, 0.6, 1.1 (b) and $\eta = 0$, 0.6, 1.1 (c). (Values for η are based on the nominal insulator thickness. The curves shown are sixth order polynomial fits to the actual data. In panel (c) every tenth data point is shown to illustrate the fit quality.)

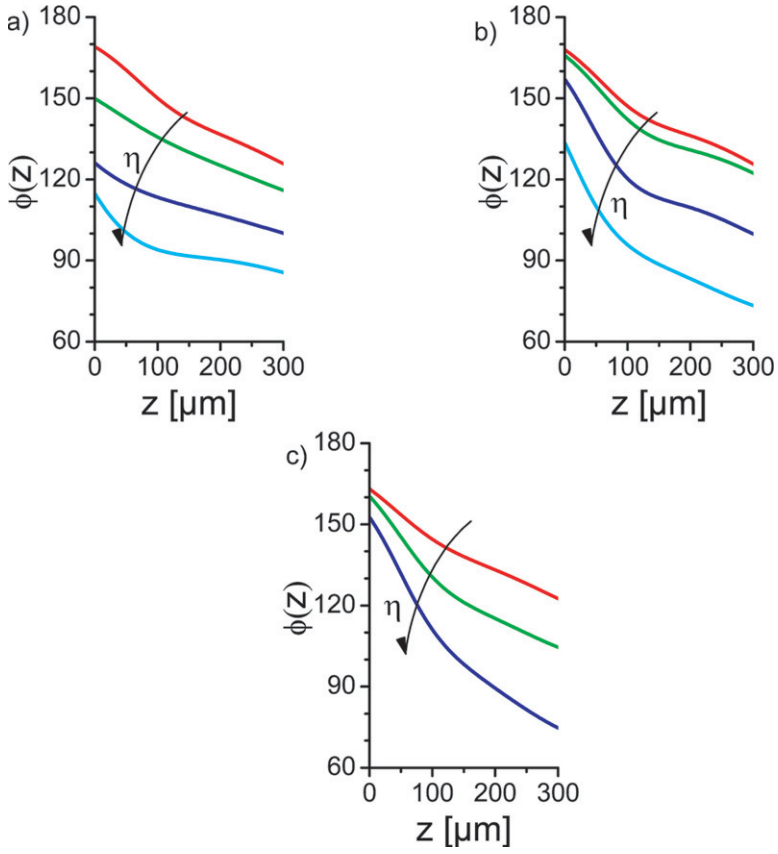

Figure 15. Local surface slope angle (w.r.t. the r-axis as indicated in figure 14(a)) versus height. Same data as in figure 14.

the details of the profiles on a scale small compared to d. For large d, however, the resolution is sufficient and the slope angle does indeed converge towards a unique, voltage-independent value of $\phi(0) \approx \theta_{Y'}$ for $z \to 0$, as theoretically predicted.

Finally, we analysed the curvature of the surface profiles. The latter was calculated by inserting the polynomial fitting coefficients into the general formula for cylindrically symmetric systems

$$\kappa = -\frac{r''}{(1+r'^2)^{3/2}} + \frac{1}{r(1+r'^2)^{1/2}}, \tag{16}$$

where the prime indicate the derivative w.r.t. z. The results are shown in figure 16. Obviously, the calculation of the second derivative strongly enhances any inaccuracy involved in the fitting procedure. This compromises the resolution and reliability of the procedure. Close to the substrate, i.e. close to the boundary of the data to be fitted, the procedure becomes particularly unreliable. Nevertheless, the data display a clear general trend: the higher the voltage, the more the curvature tends to increase for $z \to 0$. The data for $d = 50$ and 150 μm display a maximum in the curvature somewhat above the substrate. Given the current resolution, we are unable to identify whether this decrease is physical or whether it is due to inaccuracies of our data analysis procedure. We note, however, that the raw images of the drops do also suggest the existence of a maximum (see figure 11).

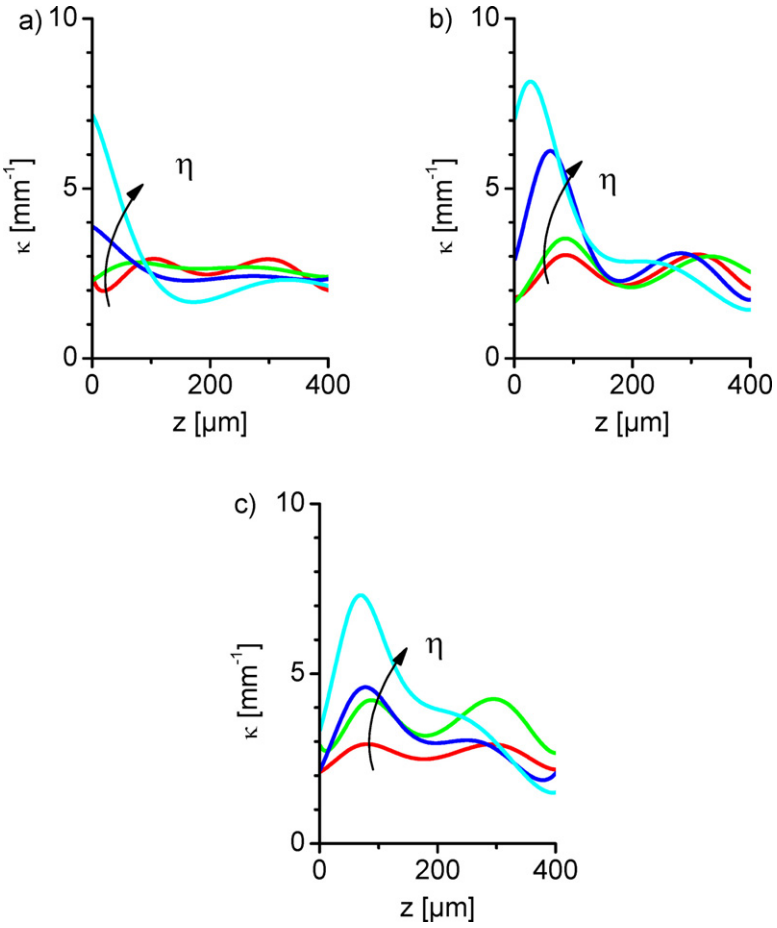

Figure 16. Curvature of the profiles in figure 14 versus height.

5. Discussion and conclusion

The experimental data presented above confirm directly the most important conclusions of our theoretical and numerical analysis: the local contact angle in electrowetting is equal to Young's angle, independent of the applied voltage. Drop surfaces are distorted (w.r.t. a spherical cap) in a range of order d around the contact line due to the high local Maxwell stress. The mean curvature of the drop surface increases for $z \to 0$. In contrast to our previous experimental attempts [30, 33], these conclusions can be drawn almost directly from the raw images. This improvement has become possible due to the choice of the specific system, which displays both a low contact angle hysteresis and, in particular, a very high Young's angle.

At first glance it may seem disappointing that the divergence of the curvature is not equally well demonstrated as the local slope. However, this is plausible for several fundamental reasons. First of all, the field enhancement close to the contact line is very weak for blunt 'tips', giving rise to an extremely weak divergence. In the present case of $\theta_Y \approx 170°$ we find $\nu \approx 0.1$ (from equation (12)). The divergence of the curvature is thus expected to be much weaker than in the numerical data presented above. Furthermore, we should note that the algebraic regime is only reached for $y < 0.01$ (cf figure 8). Even for the thickest substrate

investigated here ($d = 250\ \mu$m), the optical resolution is only of order $0.01d$. Finally, we should also note that the experimental drops are three dimensional and cylindrically symmetric and have a finite radius, whereas our numerical system represents an ideal two-dimensional system with infinite drop size. Future detailed studies of the field enhancement effect close to the contact line should take these considerations into account when choosing the experimental system as well as the experimental and numerical techniques.

The results presented here demonstrate clearly that electrowetting is in essence an electromechanical effect, as pointed out earlier (e.g. [29]). In our theoretical analysis, the interfacial tensions are assumed to be independent of the applied voltage. Electrical effects enter the problem exclusively via the Maxwell stress Π_{el} in the force balance equation (equation (3)) of the drop surface, while the electric contribution f_{el} to the force balance at the contact line (equation (4)) vanishes. (In fact, this result is in line with general arguments of variational calculus [34]: body forces, such as electrostatic forces, do not contribute to the force balance at the contact line.) However, if we minimize the total free energy of the system on the global scale (figures 4 and 5), consisting of both electrostatic and surface energy, we recover the basic electrowetting equation (equation (1)). On a global scale, the effect of the local electrostatic pressure on the liquid surface thus sums up to a net force effectively pulling on the contact line—in agreement with the general concept of the Maxwell stress tensor calculus [27]. Our numerical results indicate that the critical distance from the contact line where the electric fields essentially die out is of order d. On scales larger than this, the electromechanical action of the local electric fields sums up to a reduction of the *effective* solid–liquid interfacial tension. This reconciles the two apparently contrasting interpretations of electrowetting.

A crucial issue concerning equilibrium properties that remains open is the origin of contact angle saturation. In contrast to all published experimental data, our numerical results for two-dimensional systems show no indication of contact angle saturation. We see two possible reasons: the first one is that we did not include the possibility of dielectric breakdown of the insulating layers, which limits the maximum voltage that can be applied (see [4] and references therein). More interestingly, the absence of saturation in an ideal two-dimensional model suggests that the shape of the surface profile in three dimensions may be important for some saturation mechanisms. Surface modes running along the contact line were found to play a role in contact line instabilities, which give rise to the ejection of satellite drops [31, 32]. Such modes do not exist in a two-dimensional model.

The independence of the local contact angle from the applied voltage is expected to have important implications for the dynamics of contact lines in electric fields. The local configuration of the drop surface close to the contact line is a crucial element of all theories of dynamic wetting. As we could show here, the actual local contact angle in typical electrowetting experiments is several tens of degrees higher than naively expected, based on the apparent contact angle. Varying the insulator thickness offers the possibility of tuning the characteristic length scale on which the surface is distorted. Depending on the value of d relative to characteristic length scales in dynamics wetting models, the relevant contact angle may be either θ_{Y} or $\theta(U)$. In a recent analysis of the spreading dynamics of water drops in ambient oil, we were able to model the entrapment dynamics of thin oil films under the drop using the apparent contact angle $\theta(U)$ [15]. This is plausible since that work was performed with dielectric layers that were thin compared to the characteristic thickness arising from the asymptotic matching condition in the classical Landau–Levich problem of dip coating. Other processes, such as contact angle hysteresis (e.g. for drops in air) can involve much shorter characteristic length scales, depending on the properties of the substrate heterogeneity. In this case, we expected that θ_{Y} rather than $\theta(U)$ is the relevant parameter for the wetting dynamics. More detailed studies of the local dynamics should ultimately provide insight

into the origin of the contact line friction parameter, that was found to be indispensable for modelling electrowetting dynamics.

Acknowledgments

We are indebted to Eko Purnomo for assistance with data analysis. Benjamin Cross is acknowledged for performing the experiments. This work was supported by the Institute for Mechanics, Process and Control (Impact) at the University of Twente and by the German Science Foundation within the priority programme 'Wetting and structure formation at interfaces'.

Appendix

In this appendix, we will compare the properties of (i) perfect conductors, (ii) electrolytes, which satisfy the linear Poisson–Boltzmann equation (we will call them in the following linear electrolytes), and (iii) nonlinear electrolytes (in particular monovalent salts). We derive the correct electrowetting number η to be used in equation (1) for all three cases. The free energy of a droplet in the electrowetting configuration (liquid droplet phase l, ambient phase v) is given by

$$E = \sigma_{\mathrm{lv}} S + (\sigma_{\mathrm{sl}} - \sigma_{\mathrm{sv}}) S^* - \Delta p V + F \tag{A.1}$$

Here, Δp equals the pressure jump across the liquid–vapour interface and σ_{lv}, σ_{sl} and σ_{sv} are the liquid–vapour, solid–liquid and solid–vapour interface tensions. S and S^* denote the areas of the liquid–vapour and liquid–solid interfaces. F contains the electrostatic contribution to the energy and is given by

$$F = -\tfrac{1}{2} \int \mathrm{d}V \, (\vec{E}(\vec{r})\vec{D}(\vec{r}) + \Delta\Pi(\Phi)). \tag{A.2}$$

The last term contains the osmotic pressure of free charges and is nonzero only in an electrolyte liquid phase. Φ is the electrostatic potential and the electric field $\vec{E}(\vec{r}) = -\nabla\Phi$. The dielectric displacement is given as $\vec{D}(\vec{r}) = \varepsilon_0 \varepsilon(\vec{r}) \vec{E}(\vec{r})$. The dielectric constant $\varepsilon(\vec{r})$ generally is different for solid, liquid (respectively denoted ε_{d}, ε_{l}) and ambient phase (equal to unity).

To a first approximation, fringe effects usually are neglected and the electrostatic energy equals that of a plate capacitor formed by droplet and electrode. The energy per unit area of this plate capacitor is interpreted as a contribution to the solid–liquid interface tension and gives rise to the electrowetting equation (equation (1)).

For the perfectly conducting liquid, the energy per unit area is given by $\varepsilon_0 \varepsilon_{\mathrm{r}} U^2/2d$ and the electrowetting number therefore equals $\eta_0 = \varepsilon_0 \varepsilon_{\mathrm{r}} U^2/2\gamma d$. In this case, $\Phi = 0$ inside the liquid phase.

For the electrolytes, the Debye length $\lambda = \kappa^{-1}$ is the penetration depth of the electrostatic potential into the liquid phase. Boundary conditions are $\Phi = 0$ asymptotically inside the liquid and $\Phi = U$ at the electrode. Furthermore, $\vec{D}$ is steady across the solid–liquid interface.

In particular, for the linear electrolyte, Φ is given by $\nabla^2\Phi = \kappa^2\Phi$, where κ is defined as $\kappa^2 = \sum_{\mathrm{i}} q_{\mathrm{i}}^2 n_{\mathrm{i}}/\varepsilon_0 \varepsilon_{\mathrm{l}} k_{\mathrm{B}} T$ with the different ion charges q_{i} and bulk densities n_{i}. k_{B} is the Boltzmann constant and T the temperature of the liquid. Solving for the potential and calculating the free energy per unit area, we get for the modified electrowetting number

$$\eta = \eta_0 \frac{\varepsilon_{\mathrm{l}} d}{\varepsilon_{\mathrm{l}} d + \varepsilon_{\mathrm{r}} \lambda}. \tag{A.3}$$

This corresponds to two serial capacitors, one with dielectric constant ε_d and thickness d and one with ε_l and λ.

For a monovalent salt, the Poisson Boltzmann equation is given by $\nabla^2\phi = \kappa^2/\nu \cdot \sinh(\nu\phi)$ with $\nu = eU/k_BT$ and $\phi = \Phi/U$. Solving and integrating for the free energy per unit area, the modified Lippmann number is given by

$$\eta = \eta_0 \cdot \left[(1-\phi_0)^2 + \frac{16}{\nu^2\lambda}\frac{\varepsilon_l d}{\varepsilon_r \lambda}\sinh^2(\nu\phi_0/4)\right]. \tag{A.4}$$

ϕ_0 is the potential at the solid–liquid interface (in units of U) and satisfies

$$1 - \phi_0 - \frac{2}{\nu}\frac{\varepsilon_l d}{\varepsilon_r \lambda}\sinh\left(\frac{\nu\phi_0}{2}\right) = 0. \tag{A.5}$$

Usually λ is orders of magnitude smaller than d. In this case $\phi_0 \approx \varepsilon_r\lambda/\varepsilon_l d$ and the linear electrolyte and monovalent salt expansions of the electrowetting number both equal

$$\eta = \eta_0\left(1 - \frac{\varepsilon_r\lambda}{\varepsilon_l d}\right). \tag{A.6}$$

Inserting numbers for typical parameters in electrowetting experiments indicates that the use of η_0 (denoted simply as η in the main body of this paper) is usually sufficient.

References

[1] Taylor G I 1964 Disintegration of water drops in an electric field *Proc. R. Soc.* A **280** 383
[2] Fenn J B, Mann M, Meng C K, Wong S F and Whitehouse C M 1989 *Science* **246** 64
[3] Darhuber A A and Troian S M 2005 Principles of microfluidic actuation by modulation of surface stresses *Annu. Rev. Fluid Mech.* **37** 425
[4] Mugele F and Baret J-C 2005 Electrowetting: from basics to applications *J. Phys.: Condens. Matter* **17** R705
[5] Sandré O, Gorre-Talini L, Ajdari A, Prost J and Silberzan P 1999 Moving droplets on asymmetrically structured surfaces *Phys. Rev.* E **60** 2964
[6] Landau L D and Lifschitz E M 1985 *Elektrodynamik der Kontinua* (*Lehrbuch der Theoretischen Physik* vol VIII) (Berlin: Akademie)
[7] Chou T 2001 Geometry-dependent electrostatics near contact lines *Phys. Rev. Lett.* **87** 106101
[8] Kang K H, Kang I S and Lee C M 2003 Wetting tension due to coulombic interaction in charge-related wetting phenomena *Langmuir* **19** 5407
[9] Buehrle J, Herminghaus S and Mugele F 2003 Interface profiles near three-phase contact lines in electric fielelds *Phys. Rev. Lett.* **91** 086101
[10] Monroe C W, Daikhin L I, Urbakh M and Kornyshev A A 2006 Electrowetting with electrolytes *Phys. Rev. Lett.* **97** 136102
[11] Lippmann G 1875 Relations entre les phénomènes électriques et capillaires *Ann. Chim. Phys.* **5** 494
[12] Quilliet C and Berge B 2001 Electrowetting: a recent outbreak *Curr. Opin. Colloid Interface Sci.* **6** 1
[13] Baret J-C and Brinkmann M 2006 Wettability control of droplet deposition and detachment *Phys. Rev. Lett.* **96** 146106
[14] Baret J-C and Mugele F 2006 Electrical discharge in capillary breakup: controlling the charge of a droplet *Phys. Rev. Lett.* **96** 016106
[15] Staicu A and Mugele F 2006 Electrowetting-induced oil film entrapment and instability *Phys. Rev. Lett.* **97** 167801
[16] Mugele F, Baret J-C and Steinhauser D 2006 Microfluidic mixing through electrowetting-induced droplet oscillations *Appl. Phys. Lett.* **88** 204106
[17] Berge B and Peseux J 2000 Variable focal lens controlled by an external voltage: an application of electrowetting *Eur. Phys. J.* E **3** 159
[18] Krupenkin T, Yang S and Mach P 2003 Tunable liquid microlens *Appl. Phys. Lett.* **82** 316
[19] Kuiper S and Hendriks B H W 2004 Variable-focus liquid lens for miniature cameras *Appl. Phys. Lett.* **85** 1128
[20] Hayes R A and Feenstra B J 2003 Video-speed electronic paper based on electrowetting *Nature* **425** 383
[21] Cho S K, Moon H J and Kim C J 2003 Creating, transporting, cutting, and merging liquid droplets by electrowetting-based actuation for digital microfluidic circuits *J. Microelectromech. Syst.* **12** 70

[22] Pollack M G, Fair R B and Shenderov A D 2000 Electrowetting-based actuation of liquid droplets for microfluidic applications *Appl. Phys. Lett.* **77** 1725
[23] Jones T B, Gunji M and Washizu M 2001 Dielectrophoretic liquid actuation and nanodroplet formation *J. Appl. Phys.* **89** 1441
[24] Yeo L Y and Chang H-C 2005 Static and spontaneous electrowetting *Mod. Phys. Lett.* B **19** 549
[25] Yeo L Y and Chang H-C 2006 Electrowetting films on parallel line electrodes *Phys. Rev.* E **73** 011605
[26] Froumkine A 1936 Couche double. Électrocapillarité. Surtension *Actualités Sci. Ind.* **373** 1
[27] Jones T B 2002 On the relationship of dielectrophoresis and electrowetting *Langmuir* **18** 4437
[28] Kang K H 2002 How electrostatic fields change contact angle in electrowetting *Langmuir* **18** 10318
[29] Jones T B 2005 An electromechanical interpretation of electrowetting *J. Microelectromech. Syst.* **15** 1184
[30] Bienia M, Vallade M, Quilliet C and Mugele F 2006 Electrical-field-induced curvature increase on a drop of conducting liquid *Europhys. Lett.* **74** 103
[31] Vallet M, Vallade M and Berge B 1999 Limiting phenomena for the spreading of water on polymer films by electrowetting *Eur. Phys. J.* B **11** 583
[32] Mugele F and Herminghaus S 2002 Electrostatic stabilization of fluid microstructures *Appl. Phys. Lett.* **81** 2303
[33] Bienia M, Mugele F, Quilliet C and Ballet P 2004 Droplets profiles and wetting transitions in electric fields *Physica* A **339** 72
[34] Finn R 1986 *Equilibrium Capillary Surfaces* (New York: Springer)